JOM, Vol. 72, No. 12, 2020
https://doi.org/10.1007/s11837-020-04439-3

Oxidation Behavior of Pack-Cemented Refractory High-Entropy Alloy

WON JUNE CHOI,[1] CHUN WOONG PARK,[1] YONGWOOK SONG,[2] HYUNJOO CHOI,[2] JONGMIN BYUN ,[3,5] and YOUNG DO KIM[1,4,6]

1.—Department of Materials Science and Engineering, Hanyang University, 222 Wangsimni-ro, Seongdong-gu, Seoul 04763, Republic of Korea. 2.—School of Materials Science and Engineering, Kookmin University, Seoul 02707, Republic of Korea. 3.—Department of Materials Science and Engineering, Seoul National University of Science and Technology, 232 Gongneung-ro, Nowon-gu, Seoul 01811, Republic of Korea. 4.—The Research Institute of Industrial Science, Hanyang University, Seoul 04763, Republic of Korea. 5.—e-mail: byun@seoultech.ac.kr. 6.—e-mail: ydkim1@hanyang.ac.kr

In this study, Al pack cementation was conducted on a high-entropy alloy (HEA), and the oxidation behavior of the pack-cemented HEA was investigated. The alloy was fabricated via powder metallurgy (PM). Al pack cementation was performed at 500°C and 800°C for up to 5 h. The microstructure was analyzed after the pack cementation process, and the phase identification was conducted. The oxidation test was conducted at 1000°C for 3 h under air atmosphere, and the detailed microstructure was investigated using various analyses. The specimen that was pack-cemented at 800°C for 5 h exhibited improved oxidation resistance, whereas the specimen that was not subjected to pack cementation and the one that was pack-cemented at 500°C for 5 h demonstrated poor oxidation resistances. Microstructure and phase analyses were used to examine the diffusion of atoms and determine the oxidation behavior with regard to atomic diffusion.

INTRODUCTION

High-entropy alloys (HEAs), which exhibit high entropies compared to other commercialized alloys, were first developed by Yeh et al.[1] HEAs are composed of five atoms or more, which have similar atomic radii and structure. Owing to their high entropies, these alloys comprise a single-phase solid solution rather than intermetallic phases.[2] HEAs are known to exhibit superior mechanical properties, such as ductility at low temperature, wear resistance, and resistance to corrosion. These properties arise from various phenomena, such as the high-entropy effect and the lattice-distortion effect.[3–6] Owing to their peculiar behavior, extensive research has been conducted on HEAs.[5,7–10] Industrial exploitation of HEAs is foreseen, for instance, in the aerospace industry, in which materials with excellent reliability and durability at high temperature are sought. HEAs can be classified into FCC (face-centered cubic)- and BCC (body-centered cubic)-based HEAs according to their crystal structure. These two types of HEAs exhibit different behaviors in terms of ductility and strength. Recently, refractory high-entropy alloys (RHEAs) based on refractory metals with high melting points (such as Mo, Nb, and W) have been researched as the next-generation high-temperature materials.[11–19] Moreover, it has been reported that RHEAs exhibit superior mechanical properties to those of some commercialized Ni-based superalloys. However, the applicability of these alloys is hindered because of its brittleness at room temperature and its inferior oxidation properties at elevated temperatures, which are a result of the intrinsic properties of its constituent refractory metals. Recently, research on eutectic HEAs (composed of a BCC or FCC phase as well as intermetallic phases) has been conducted with the aim of improving ductility while minimizing the reduction of strength.[20–23] In addition, medium-entropy alloys (MEAs), characterized by configurational entropies at random states

(Received June 20, 2020; accepted October 5, 2020; published online October 27, 2020)

between 1 R and 1.5 R ($1R \leq \Delta S_{conf} \leq 1.5R$), have been investigated as they can offer enhanced mechanical properties.[24,25] Furthermore, RHEAs were reported to exhibit ductility at room temperature by Sheikh et al. and other research groups [26–32]; however, oxidation properties of RHEAs were not addressed because refractory metals tend to get oxidized easily at high temperatures. As a result, the potential of coating the surfaces of RHEAs to prevent their oxidation was evaluated; consequently, pack cementation coating could be an effective way to limit the oxidation at high temperatures.[33] However, the oxidation mechanism of pack-cemented RHEAs has been unclear thus far. Furthermore, it is estimated that the oxidation behavior varies significantly, depending on the elements of the RHEAs; this is because a plethora of HEAs can be designed with different compositions depending on the constituent elements. As a result, oxidation properties of each HEA must be studied individually to elucidate the fundamental oxidation mechanism.

In this study, we investigated the oxidation properties of CrMoNbTaW RHEA and determined its oxidation mechanism. The CrMoNbTaW RHEA was fabricated using high-energy ball milling and spark plasma sintering (SPS). Subsequently, this alloy was pack-cemented, and an oxidation test was also conducted. A detailed investigation about its microstructure was performed to verify the oxidation mechanism of Al pack-cemented RHEAs.

EXPERIMENTAL PROCEDURES

Pure Cr (99.9%, RND KOREA, Korea), Mo (99.9%, RND KOREA, Korea), Nb (99.9%, RND KOREA, Korea), Ta (99.95%, RND KOREA, Korea), and W (99.9%, RND KOREA, Korea) powders were prepared to fabricate the high-entropy powder. The powder was weighed to meet the nominal composition, which was set to have an atomic ratio of Cr:Mo:Nb:Ta:W = 1:1:1:1:1. Subsequently, 100 g of powder was placed into a milling jar (SKD 11) under Ar atmosphere. Stainless balls (SUS304) with a diameter of 4.765 mm were added with a ball-to-powder ratio (BPR) of 10:1 (wt.%). Then, 0.1 wt.% (0.1 g in this research) stearic acid (99%, SAMCHUN, Korea) was added as a process control agent (PCA) to avoid cold welding of the powders. A planetary milling machine (PM400, RETSCH) was used for high-energy ball milling at 200 rpm for up to 30 h, alternating 10 min of milling with 5 min of rest. A small amount of milled powder was sampled after each hour of milling for x-ray diffraction (XRD, miniFlex600, RIGAKU, installed at Hanyang LINC+ Analytical Equipment Center, Seoul) and scanning electron microscope (SEM, SU8010, HITACHI) analyses. Finally, the HEA was fabricated using the milled powder via the SPS (SPS-632Lx, FUJI ELECTRONIC INDUSTRIAL CO.) process, wherein the sintering process was conducted at 1600°C under 50 MPa pressure for 20 min in an Ar atmosphere.

The powders for pack cementation were prepared, which comprised Al (99.9%, KOJUNDO, Japan) as a diffusion source, Al_2O_3 (99.9%, KOJUNDO, Japan) as an inert filler, and NH_4Cl (99%, DUKSAN, Korea) as a halide activator. These powders were mixed for 10 h via a 3D shaker-mixer (Turbula, WAB) to mix the powder uniformly. Subsequently, the mixed powder was placed into the alumina crucible, and the machined and polished HEA specimen was buried in this powder. The packed crucible was heat-treated using an electric furnace at 500°C and 800°C for up to 5 h in Ar atmosphere.

The pack-cemented HEA specimens were oxidized in the electric furnace at 1000°C for 3 h in an air atmosphere, and the HEA specimen that was not pack-cemented was also oxidized under the same conditions. A XRD was used to confirm the fabrication of the high-entropy powder and check the phase transformation at each process. A SEM was also used to analyze the morphology of the powder and the microstructures of the pack-cemented HEA and oxidized HEA. In addition, the diffusion of the atom was roughly estimated using an energy-dispersive spectrometer (EDS). The name of the specimen at each step is given in Table I.

RESULTS AND DISCUSSION

Herein, the pure Cr, Mo, Nb, Ta, and W powders had been ball-milled to fabricate the HEA, and its XRD patterns are shown in Fig. 1a. Progressive decreases in peak intensity and peak broadening were only observed during the first hour of milling, implying that mechanical alloying (MA) progressed during the early stage of milling. After 5 h of milling, the peaks of the pure powder were not observed in the XRD patterns. When the ball milling had been carried out for 30 h, the peaks of the BCC phase were observed, while the peak intensity significantly decreased compared to that seen in the initial milling stage. In addition, a small number of peaks was also observed. It was assumed that these peaks corresponded to a Ta-rich phase (shown in black in Fig. 1c). This phase was formed during the milling process because of thermodynamic stability. However, the small height of the peaks suggested that the proportion of this phase was small. As a result, the powder that was ball-milled for 30 h was used to fabricate the HEA in this research.

Figure 1b is a SEM image of the HEA after SPS process at 1600°C for 20 min. Here, it seems that the as-SPSed HEA had a clear microstructure, and the pore was not observed. However, when we investigated the microstructure using high magnification as shown in Fig. 1c, several black dots were observed with a size of 2 μm or less. Mapping was conducted by EDS analysis, and the distribution of

Table I. Names of the specimens used in this research depending on whether they were subjected to pack cementation and oxidation

	Pack cementation		Oxidation	
Sample	**Temperature (°C)**	**Holding time (h)**	**Temperature (°C)**	**Holding time (h)**
HEA	–		–	
HEA_O	–		1000	3
PC500_1h	500	1		
PC500_3h	500	3		
PC500_5h	500	5		
PC800_1h	800	1		
PC800_3h	800	3		
PC800_5h	800	5		
PC500_5h_O	500	5	1000	3
PC800_5h_O	800	5	1000	3

the different HEA elements is shown in Fig. 1d–h for Cr, Mo, Nb, Ta, and W, respectively. The EDS mapping and point analyses (as shown in supplementary Fig. S-1 and Table S-I) of the identified phase were observed to correspond with those of Cr, Ta, and W and did not match with those of Mo and Nb. It was assumed that the absence of Mo and Nb was occurred during a high-energy ball-milling process or SPS process; however, the formation mechanism of the Ta-rich phase remained unclear. An additional study related to the optimization of the milling and sintering processes must be conducted to obtain a superior microstructure with a single BCC phase. Al pack cementation was conducted using the machined and polished HEA by following the above-mentioned experimental procedure.

Figure 2 represents the results of the XRD and SEM analyses after the Al pack cementation. The XRD patterns of the as-SPSed HEA specimen and the specimens subjected to pack cementation at 500°C (PC500_1h, PC500_3h, and PC500_5h) and 800°C (PC800_1h, PC800_3h, and PC800_5h) for up to 5 h were shown in Fig. 2a. In Fig. 2a, the PC500 specimen exhibited BCC and Ta-rich phases, which were also observed in the ball-milled powder. In addition, the XRD patterns of the specimens that were pack-cemented at 500°C for up to 5 h did not differ from that of the as-SPSed HEA specimen. This meant that the HEA did not react with the Al coating layer because a diffusion at the interface between the HEA and the Al coating layer rarely occurred because of the relatively low temperature. In contrast, the PC800 specimens exhibited different peaks compared to those of the PC500 specimens. The PC800_1h specimen had a significantly different XRD pattern compared to that of the as-SPSed HEA. New phases, such as $AlNb_3$, Al_3Ta, and Al_4W, were observed in the phase-searching program. They formed through a reaction between the HEA and the Al coating layer; however, identifying an exact phase was difficult owing to the peak similarity of the new phases ($AlNb_3$, Al_3Ta, Al_4W, and so on) in the XRD patterns. Therefore, these phases were named as the $Al(Cr,Mo,Nb,Ta,W)_x$ phase. These phases were also detected in the PC800_3h and PC800_5h specimens, which implied that the reaction between HEA and the Al coating layer readily occurred at 800°C. Figure 2b is a cross-sectional SEM image of the PC500_5h specimen, wherein a thin Al coating layer existed on the surface of HEA. Its magnified image has been shown in Fig. 2c, wherein the Al coating layer exists as a non-dense layer with a thickness of about 2 μm. Each layer was investigated by carrying out the EDS point analysis quantitatively (as shown in Fig. S-2 and Table II). In Fig. 2c and d, we marked five regions as cross marker 1 to cross marker 7 and termed them as point 1 to point 7, respectively. Only Al and O elements were detected at point 1, and the area of points 2 and 3 was analyzed to be the HEA. The Al coating layer was not observed in the PC500_1h and PC500_3h specimens because of insufficient temperatures and holding times. In specimens that were subjected to pack cementation at 800°C for up to 5 h, the Al coating layer was observed on the surface of the HEA, and the average thickness of the layer on the PC800_1h, PC800_3h, and PC800_5h specimen was approximately 28.7 μm, 37.9 μm, and 44.3 μm, respectively. Figure 2d is a cross-sectional SEM image of the PC800_5h specimen, and Fig. 2e is a magnified SEM image of the region between the HEA and the Al coating layer. As shown in Fig. 2d, the dense Al coating layer with a thickness of 44.3 μm exists on the surface of the HEA. In the area of points 4 and 5, Al and O elements were detected along with the HEA elements (about 1–4 at%) because of the diffusion of the HEA elements. The HEA elements with similar ratios were analyzed in each point 6 and 7, wherein Al was not detected. In Fig. 2e, the Ta-rich phase observed in Fig. 1c is also detected. The diffusion of HEA elements into the Al coating layer was observed via the EDS point and mapping

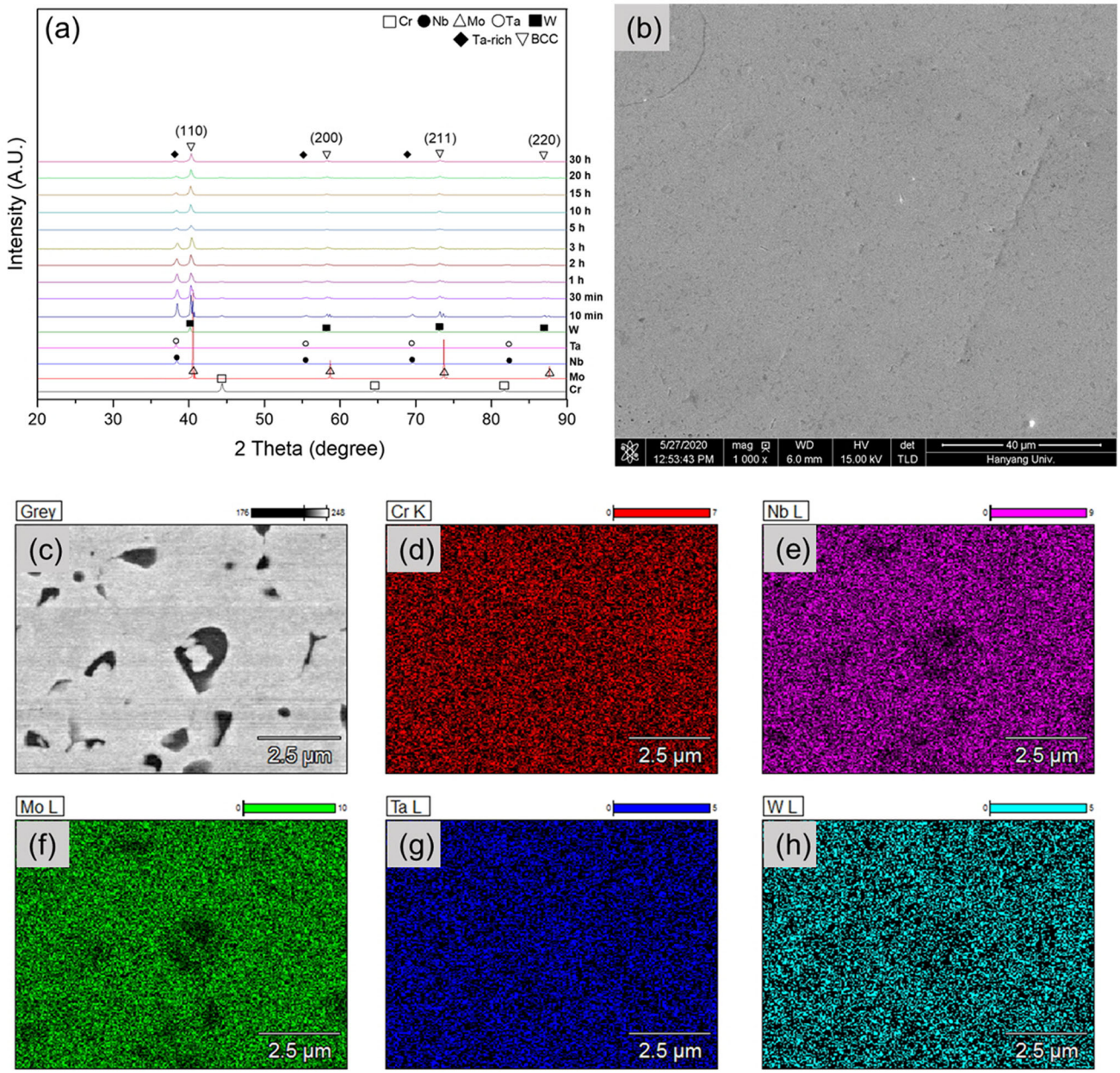

Fig. 1. (a) XRD patterns of the high-entropy powder that was milled for up to 50 h. (b) SEM image of the HEA that was SPSed at 1600°C for 20 min. Results of the EDS mapping analysis: (c) magnified SEM image, mapping of (d) Cr, (e) Nb, (f) Mo, (g) Ta, and (h) W.

analysis, whereas Al was not observed to diffuse into the HEA. The effect of the HEA elements on the oxidation mechanism was investigated in subsequent oxidation tests.

The HEA, PC500_5h, and PC800_5h specimens were oxidized at 1000°C for 3 h under an air atmosphere. Their images were captured after the oxidation test and are shown in Fig. 3a. The HEA_O specimen was almost completely oxidized, and the specimen was damaged because of the crack caused by oxidation at a high temperature and subsequent cooling. The PC500_5h_O specimen was also oxidized; however, it seemed that the effect of oxidation was not as severe as that of the HEA_O specimen. Conversely, PC800_5h_O was hardly oxidized except for a small part of the oxidized region at the surface; its original shape was also unchanged after oxidation. This is a result of the protection provided by the Al coating layer because of the pack cementation, as shown in Fig. 2d. To investigate the resulting oxidation behavior and mechanism, the microstructure of the oxidized HEA (HEA_O) specimen was analyzed in detail using SEM, and its result is shown in Fig. 3b–j. After separating the oxide layer and HEA as shown in Fig. 3a, the reminder of the HEA region was investigated using SEM analysis, and the results are shown in Fig. 3b and c. In SEM images, the oxide layer with

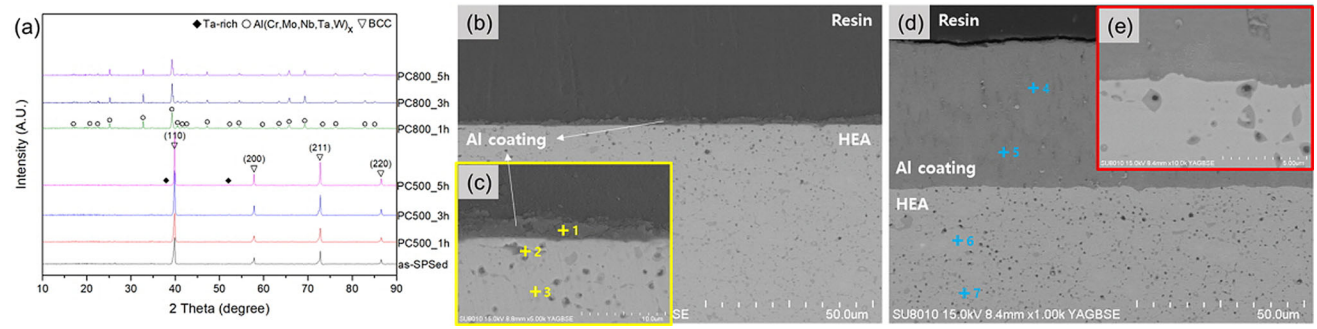

Fig. 2. (a) XRD patterns of the specimen subjected to Al pack cementation at 500°C and 800°C for up to 5 h, (b) SEM image of the PC500_5h specimen, (c) magnified SEM image of the PC500_5h specimen with points where the regions were analyzed using EDS point analysis, (d) SEM image of the PC800_5h specimen with points where the regions were analyzed using EDS point analysis, and (e) magnified SEM image of the PC500_5h specimen.

approximately 50 μm thickness was observed to exist even after the separation, and its surface had become rough because of the formation of the crack. It was assumed that the micro-crack caused by the difference between the coefficients of the thermal expansion occurred during the furnace cooling. The crack also leads to the separation of the oxide layer and the HEA, as shown in Fig. 3a. In Fig. 3b and c, it seems that the oxide layer has penetrated into the HEA region. In addition, a diffusion zone was observed between the oxide layer and the HEA in Fig. 3d. To investigate the distribution of each atom, EDS mapping analysis has been conducted, and its results are shown in Fig. 3e–j. The penetrated oxide layer comprised the Ta and O elements while the diffusion area was covered with the Cr, Mo, Nb, and W elements. Ta had a relatively high oxygen solubility compared to other HEA elements.[34–38] This meant that Ta had a large amount of oxygen content compared to the other elements in this study; however, it did not form the Ta_2O_5 phase, which was a stable phase among tantalum oxides. In addition, the distribution of Cr was antithetic to the distribution of Ta as Cr was mainly detected at the diffusion region. It was assumed that Cr diffused from the HEA and subsequently concentrated at the diffusion zone, which is located at the interface between the oxide layer and the HEA. As the oxidation proceeded, HEA elements such as Cr, Mo, Nb, and W were also oxidized and formed complex oxides [termed (Cr,Mo,Nb,Ta,W)O_x].

The PC500_5h_O (oxidized PC500_5h) specimen is also separated into several parts like the HEA_O specimen, as shown in Fig. 3a; furthermore, it was analyzed, and the corresponding results are shown in Figs. 4 and 5. Figure 4a represents the SEM image of the top view of the PC500_5h_O specimen immediately after oxidation. It had a rough surface because of the crack caused by oxidation and subsequent furnace cooling; subsequently, the EDS point analysis (as shown in supplementary Fig. S-3 and Table S-III) was conducted. In points 1 and 2 shown in Fig. 4b, the Cr- and Mo-depleted oxide was detected, whereas in points 3 and 4, the (Cr,Mo,Nb,Ta,W)O_x complex oxide was observed. In Fig. 5, the cross-sectional SEM images are shown. As shown in Fig. 5a, despite of the separation of the oxide layer from HEA as shown in Fig. 3a, the oxide layer, which had a thickness of 1 mm, was observed to still remain on the surface of HEA. The outer region of the oxide layer is shown in Fig. 5b and c; subsequently, the EDS point analysis (as shown in supplementary Fig. S-4 and Table S-IV) was also conducted. Each phase in Fig. 5b was determined to be the oxide phase. The (Nb,Ta,W)O_x complex oxide was detected at the region of point 1 in Fig. 5c, and its result was similar to those of points 1 and 2 in Fig. 4b. In addition, the region of point 2 in Fig. 5c was observed to correspond to the regions of point 3 and 4 in Fig. 4b; the (Cr,Mo,Nb,Ta,W)O_x complex oxide was detected in this region. When considering the microstructure of both oxide phases, it was assumed that the diffusion of oxygen occurred through the relatively porous (Nb,Ta,W)O_x complex oxide rather than the (Cr,Mo,Nb,Ta,W)O_x complex oxide. This made the oxygen penetrate into the inner region of specimen, and the oxidation continued. However, the formation mechanisms of these complex oxides remain unclear; therefore, it is necessary additionally to study the oxidation behavior and mechanism that relates to the addition of Cr in HEA. Figure 5d represents a magnified image of the interface between the oxide layer and the HEA, which separated because of the crack. The inner oxide layer in close proximity to the HEA has been investigated; the corresponding results are shown in Fig. 5e. In Fig. 5e, only the (Cr,Mo,Nb,Ta,W)O_x oxide is detected. Subsequently, the HEA region was examined, and its results are shown in Fig. 5f. The EDS point analysis (as shown in supplementary Fig. S-3 and Table S-III) revealed that the region of point 3 had a similar composition to that of the region in Fig. 5e. The region of point 4 and 5 was analyzed as a HEA with a similar atomic ratio compared to those of the HEA elements. Figure 6 is a surface SEM image of the PC800_5h_O (oxidized PC800_5h) specimen obtained immediately after

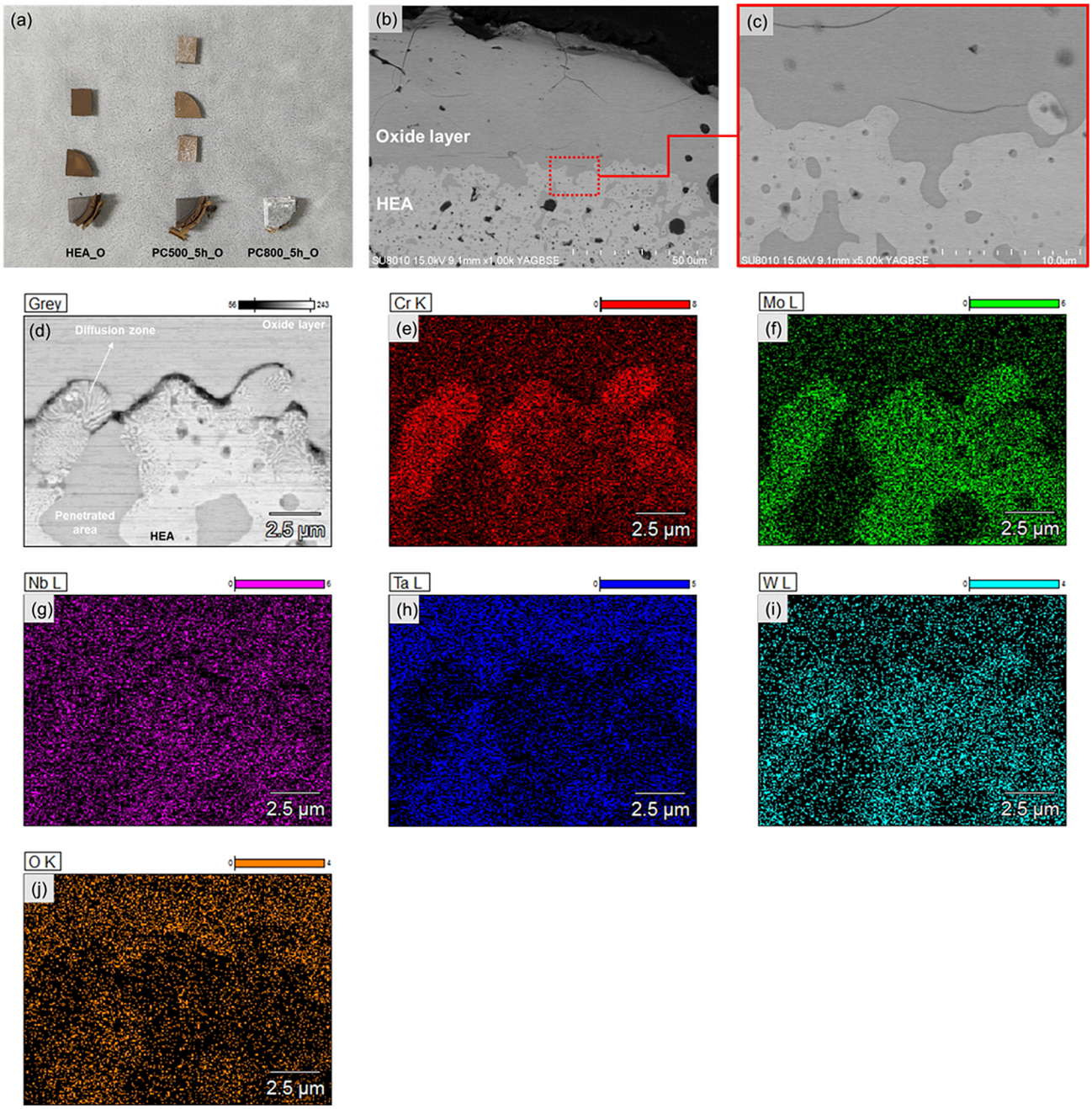

Fig. 3. (a) Image of the HEA_O, PC500_5h_O, and PC800_5h_O specimens after oxidation. Cross-sectional SEM images of the HEA_O specimen, which were not pack-cemented but oxidized at 1000°C for 3 h: (b) overall image of the specimen after oxidation, (c) magnified image of the interface between the oxide layer and the HEA region, (d) image of the cracked region between the oxide layer and HEA region, and (e)-(j) EDS mapping images of Cr, Mo, Nb, Ta, W, and O, respectively.

oxidation. The PC800_5h_O specimen did not disintegrate into an oxide layer and HEA, as shown in Fig. 3a. In Fig. 6a, the PC800_5h_O specimen exhibits a rough and sharp surface. In the magnified image shown in Fig. 6b, the needle shape of the phase was formed on the surface of the PC800_5h_O specimen; this phase was analyzed as a pure Al oxide phase. In some regions, a white powder was detected as shown in Fig. 6c; the EDS point analysis confirmed that this powder was indeed the $(Al,Cr,Mo,Nb,Ta,W)O_x$ complex oxide (as shown in supplementary Fig. S-5 and Table S-V). The PC800_5h_O specimen was polished and observed to elucidate the microstructure. Figure 7 is a cross-sectional SEM image of the PC800_5h_O specimen. As shown in Fig. 7a, the layer was evidently distinguished to comprise the oxide layer and the HEA; furthermore, a diffusion zone was also observed between the oxide layer and the HEA. After surface oxidation, a diffusion zone was formed

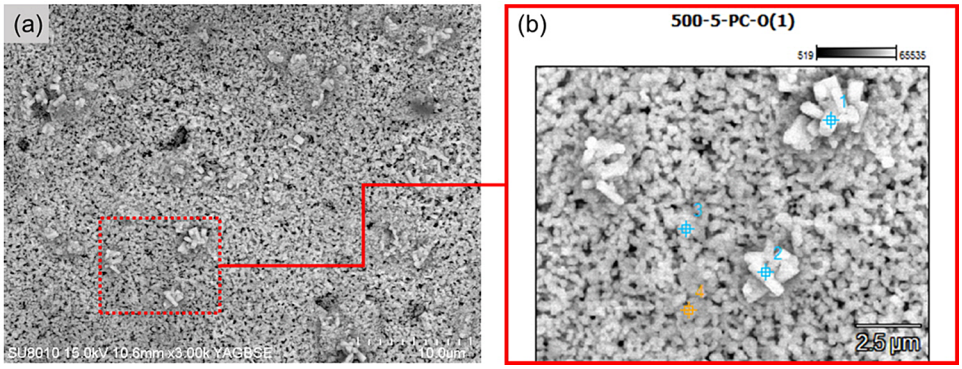

Fig. 4. Top-view images of the PC500_5h_O specimen, which was pack-cemented at 500°C for 5 h and subsequently oxidized at 1000°C for 3 h: (a) overall image of the specimen after oxidation without any sample preparation and (b) magnified image of the oxide region with points where the region was analyzed using EDS point analysis.

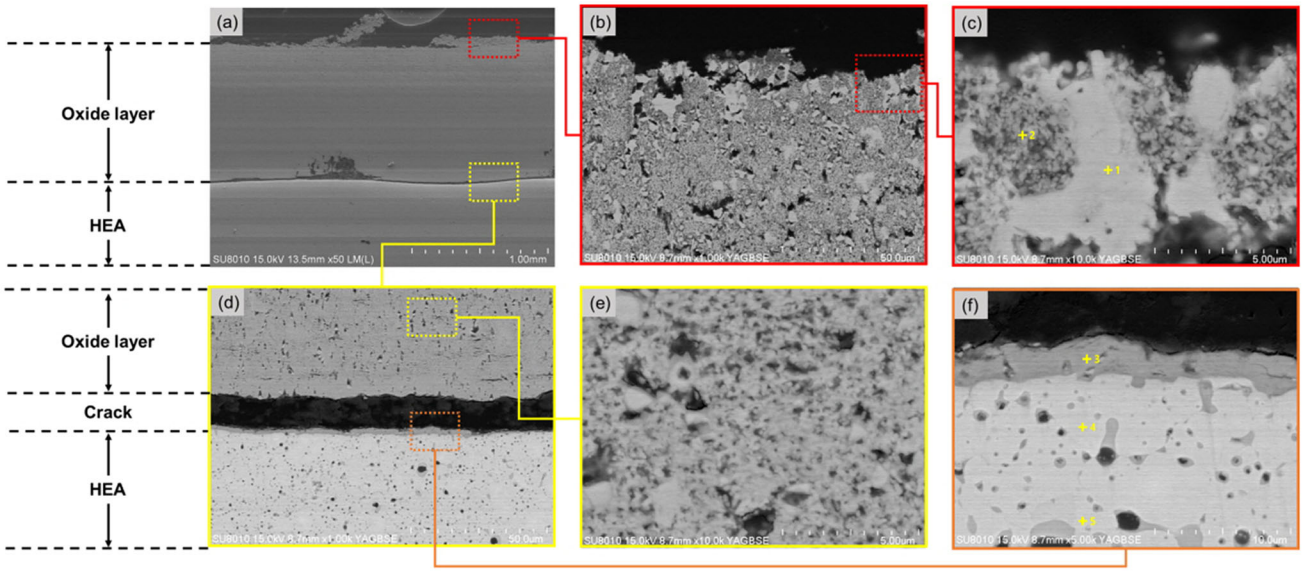

Fig. 5. Cross-sectional SEM images of the PC500_5h_O specimen, which was pack-cemented at 500°C for 5 h and subsequently oxidized at 1000°C for 3 h: (a) overall image of the specimen after oxidation, (b) image of the surface region of the oxide layer, (c) magnified image of the surface region of the oxide layer with points where the region was analyzed using EDS point analysis, (d) image of the cracked region between the oxide layer and the HEA region due to the oxidation, (e) magnified image of the inner region in the oxide layer, and (f) magnified image of the cracked region with points where the region was analyzed using the EDS point analysis.

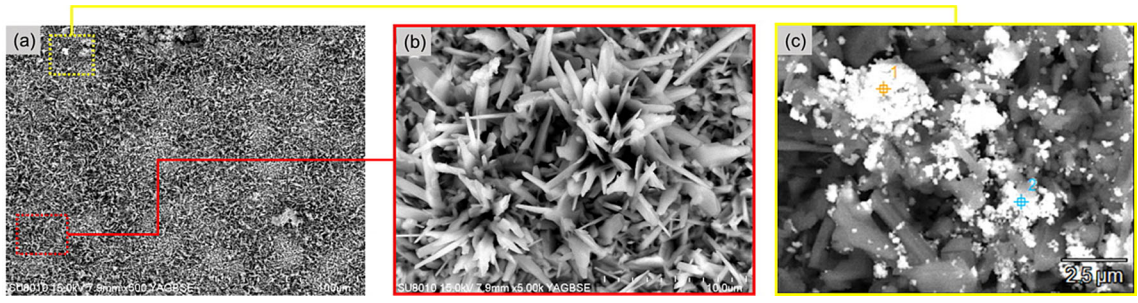

Fig. 6. Top-view images of the PC800_5h_O specimen, which was pack-cemented at 800°C for 5 h and subsequently oxidized at 1000°C for 3 h: (a) overall image of the specimen after oxidation without any sample preparation, (b) magnified image of the Al oxide region with points where the region was analyzed using EDS point analysis, and (c) magnified image of the HEA oxide region with points where the region was analyzed using EDS point analysis.

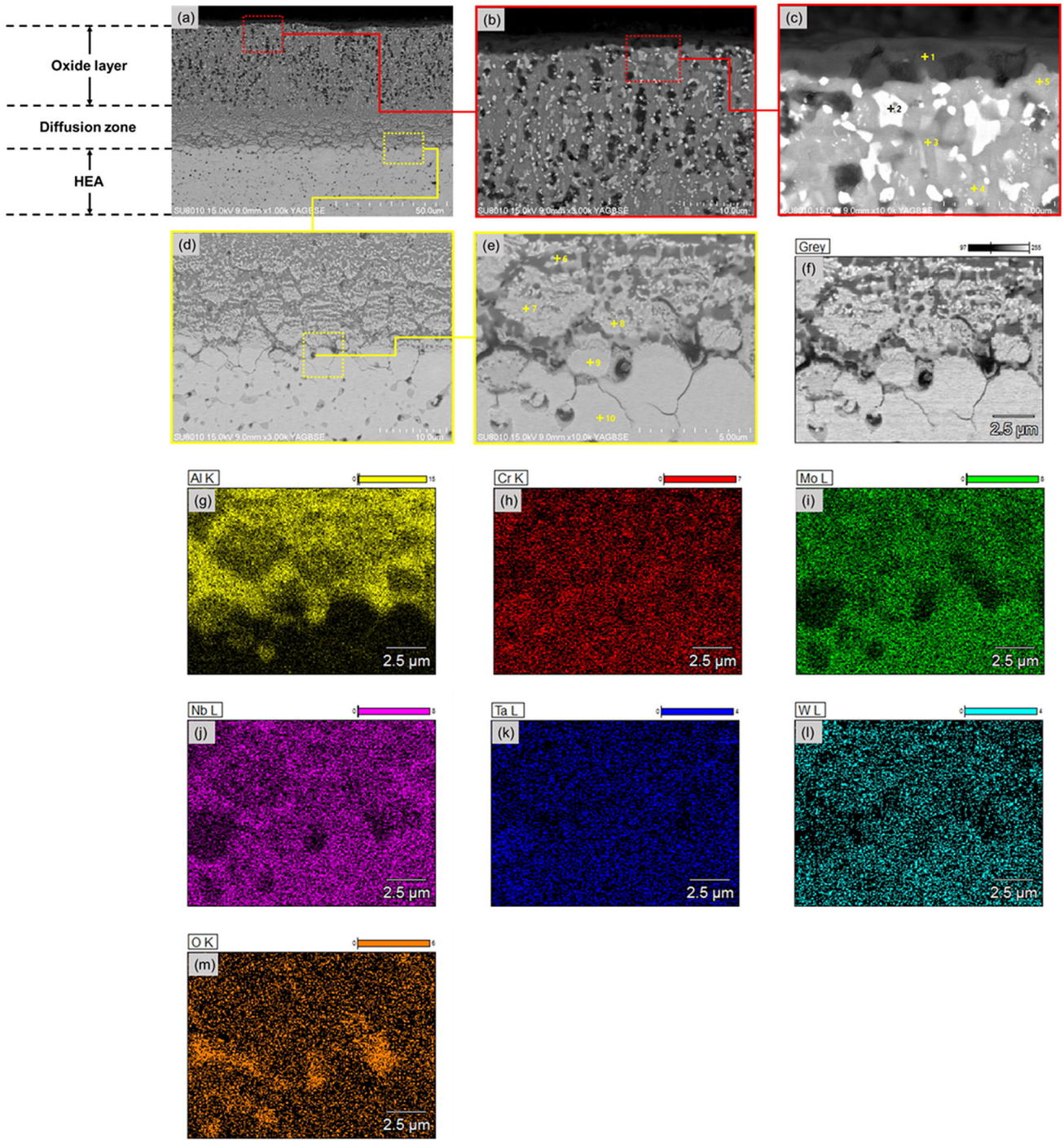

Fig. 7. Cross-sectional SEM images of the PC800_5h_O specimen, which was pack-cemented at 800°C for 5 h and subsequently oxidized at 1000°C for 3 h: (a) overall image of the specimen after oxidation, (b) image of the surface region of the oxide layer, (c) magnified image of the surface region of the oxide layer with points where the region was analyzed using EDS point analysis, (d) image of the interface between the diffusion zone and HEA region, (e) magnified image of the interface between the diffusion zone and the HEA region with points where the region was analyzed using EDS point analysis, and (g)-(m) EDS mapping images of Al, Cr, Mo, Nb, Ta, W, and O, respectively.

by the diffusion of oxygen from the surface to the HEA and the diffusion of the HEA elements to the oxide layer. In Fig. 7b, which is a magnified image of the outer region of the oxide layer, a thin layer with 2 μm thickness or less is observed at the outermost surface of the oxide layer; herein, several oxide phases colored white, gray, and black exist uniformly under the thin layer. The EDS point analysis (as shown in supplementary Fig. S-6 and Table S-VI) was conducted as shown in Fig. 7c. The region of point 1 was determined to be pure Al oxide, which corresponded with the result of Fig. 6b. In the

region of point 2, the (Al,Cr,Ta,W)O_x complex oxide phase that led to the depletion of Mo and Nb was confirmed, and regions of points 3, 4, and 5 were analyzed to be the (Al,Cr,Mo,Nb,Ta,W)O_x complex oxide. These complex oxides were formed because of the diffusion of HEA elements to the oxide layer and the diffusion of oxygen from the surface to the oxide layer. However, the amount of oxygen at point 4 was significantly low at about 14 at%. This is caused by a barrier to oxygen diffusion, which is a result of the dense Al oxide layer at the outermost surface of the oxide layer. Consequently, the PC800_5h_O specimen was not severely oxidized compared to the HEA_O and PC500_5h_O specimens. Figure 7d is a SEM image of the diffusion zone between the oxide layer and HEA, and its magnified image is shown in Fig. 7e. In the region of point 6 as shown in Fig. 7e, Al was detected numerous times, along with the HEA and O. This region was assumed to be the Al-rich (Al,Cr,Mo,Nb,Ta,W)O_x complex oxide. In the regions of points 7 and 8, the Al-rich (Al,Cr,Mo,Nb,Ta,W)O_x complex oxide was also detected; however, the amount of Al was low compared to that in the region of point 6. The phase at points 9 and 10 was confirmed to be a BCC phase. Considering the thickness of the original Al coating layer of approximately 45 μm thickness as shown in Fig. 2d, the upward and downward diffusion of Al and the HEA elements occurred at the interface between the Al coating layer and the HEA, respectively. However, when considering the EDS point analysis in Fig. 7c and e, HEA elements diffused from the interface to the surface of the oxide layer, while Al rarely diffused into the HEA from the interface. To determine the overall diffusion tendency of each elements, additional EDS mapping was conducted as shown in Fig. 7f; the mapping results of Al, Cr, Mo, Nb, Ta, W, and O elements are shown in Fig. 7g–m, respectively. As a result of the SEM image and the EDS point and mapping analysis, it seemed that the crack through the grain boundaries observed in the lower diffusion zone (Fig. 7e) occurred because of the formation of the Ta-rich oxide. After cracking, Al was observed to diffuse through the grain boundaries as shown in Fig. 7f and g. As the oxidation continued, the HEA regions were surrounded by grain boundaries, and the isolated HEA was formed as shown in the region of point 9. This isolated HEA was continuously oxidized with Al and O, and a complex oxide phase ((Al,Cr,Mo,Nb,Ta,W)O_x) was formed as shown in Fig. 7b. As a result, the number of isolated HEA regions decreased as when observing the diffusion zone from bottom to top. This phenomenon was able to explain the formation of three layers, which are shown in Fig. 7a. Compared to HEA_O and PC500_5h_O, PC800_5h_O was not oxidized severely when considering the appearance after oxidation and thickness of the oxide layer. In addition, the concentration of Ta, which was shown in HEA_O, and Cr and Mo depleted complex oxide in PC500_5h_O was not observed in the PC800_5h_O specimen. This was mainly caused by the protective Al coating layer in the PC800_5h specimen, and especially the outermost Al oxide layer and the dense (Al,Cr,Mo,Nb,Ta,W)O_x phase, which inhibited the penetration of oxygen from the surface. Refractory metals are well known because of the oxidation characteristic at high temperature. Mo and W easily transformed Mo oxide and W oxide at high temperature, respectively; these oxides evaporated as a gaseous phase. Nb and Ta are also oxidized at high temperature and form a solid oxide phase. However, the CrMoNbTaW RHEA in this study showed the complicated oxidation behavior due to the interaction of each atom. HEA and PC500_5h specimens showed catastrophic oxidation due to the continuous penetration of oxygen, whereas the PC800_5h_O specimen showed the improved oxidation properties compared to the other specimen. It also showed the reaction with the Al coating layer, and the oxidation resistance was improved. In this study, Al pack cementation had a positive effect on oxidation resistance at 1000°C. As a result, the protective Al coating layer could be an essential process to hinder the oxidation of RHEA. A further study focused on the interaction between the Al coating layer and RHEA should be investigated to improve the oxidation resistance.

CONCLUSION

In this study, CrMoNbTaW HEA was fabricated via a PM method, and Al pack cementation was conducted on the HEA. The oxidation behavior of the alloy was investigated using various analyses. The oxidation behavior of the HEA and the pack-cemented HEA was also elucidated.

1. HEA was fabricated via high-energy ball milling, which was followed by the SPS process. It was mainly composed of the BCC phase, while the Ta-rich phase was also detected.
2. Pack cementation was conducted at 500°C and 800°C for up to 5 h. The specimens that were pack-cemented at 500°C did not comprise enough Al coating layer due to the insufficient temperature and holding time. PC800_1h, PC800_3h, and PC800_5h specimens had an Al coating layer with 28.7 μm, 37.9 μm, and 44.3 μm thickness, respectively, while comprising an Al(Cr,Mo,Nb,Ta,W)$_x$ complex phase.
3. Both the HEA_O and PC500_5h_O specimens were damaged by the crack at the interface between the oxide layer and the HEA. It seemed that the Ta had a huge amount of oxygen compared to other elements, and it caused the continuous oxidation of HEA. In addition, complex oxide phases such as (Nb,Ta,W)O_x and (Cr,Mo,Nb,Ta,W)O_x were formed, and it affected the oxidation resistance of alloy.
4. PC800_5h_O had better oxidation resistance due to the protective Al oxide layer at the

outermost surface. In addition, a relatively dense oxide layer with various complex oxides was formed by the reaction between the Al oxide layer and HEA elements. However, due to the penetration of Al atoms through the grain boundaries in the diffusion zone, isolated HEA was formed, and subsequently HEA was oxidized because of the reaction with Al and O.

ACKNOWLEDGEMENTS

This research was supported by the Basic Science Research Program through the National Research Foundation of Korea (NRF) funded by the Ministry of Education (NRF-2016R1A6A1A03013422 and 2018R1D1A1A09084113).

CONFLICT OF INTEREST

On behalf of all authors, the corresponding author states that there is no conflict of interest.

ELECTRONIC SUPPLEMENTARY MATERIAL

The online version of this article (https://doi.org/10.1007/s11837-020-04439-3) contains supplementary material, which is available to authorized users.

REFERENCES

1. J.-W. Yeh, S.K. Chen, S.J. Lin, J.Y. Gan, T.S. Chin, T.T. Shun, C.H. Tsau, and S.Y. Chang, *Adv. Eng. Mater.* 6, 299 (2004).
2. Y.F. Ye, Q. Wang, J. Lu, C.T. Liu, and Y. Yang, *Mater. Today* 19, 349 (2016).
3. J.-W. Yeh, *Ann. Chim. Sci. Mater.* 31, 633 (2006).
4. M.H. Chuang, M.H. Tsai, W.R. Wang, S.J. Lin, and J.W. Yeh, *Acta Mater.* 59, 6308 (2011).
5. B. Gludovatz, A. Hohenwarter, D. Catoor, E.H. Chang, E.P. George, and R.O. Ritchie, *Science* 345, 1153 (2014).
6. T. Fujieda, H. Shiratori, K. Kuwabara, M. Hirota, T. Kato, K. Yamanaka, Y. Koizumi, A. Chiba, and S. Watanabe, *Mater. Lett.* 189, 148 (2017).
7. Z. Li, K.G. Pradeep, Y. Deng, D. Raabe, and C.C. Tasan, *Nature* 534, 227 (2016).
8. Y. Zou, H. Ma, and R. Spolenak, *Nat. Commun.* 6, 7748 (2015).
9. C. Niu, C.R. LaRosa, J. Miao, M.J. Mills, and M. Ghazisaeidi, *Nat. Commun.* 9, 1363 (2018).
10. E.P. George, D. Raabe, and R.O. Ritchie, *Nat. Rev. Mater.* 4, 515 (2019).
11. O.N. Senkov, G.B. Wilks, D.B. Miracle, C.P. Chuang, and P.K. Liaw, *Intermetallics* 18, 1758 (2010).
12. O.N. Senkov, G.B. Wilks, J.M. Scott, and D.B. Miracle, *Intermetallics* 19, 698 (2011).
13. O.N. Senkov, S.V. Senkova, D.M. Dimiduk, C. Woodward, and D.B. Miracle, *J. Mater. Sci.* 47, 6522 (2012).
14. O.N. Senkov, S.V. Senkova, C. Woodward, and D.B. Miracle, *Acta Mater.* 61, 1545 (2013).
15. Y. Zou, S. Maiti, W. Steurer, and R. Spolenak, *Acta Mater.* 65, 85 (2013).
16. C.M. Liu, H.M. Wang, S.Q. Zhang, H.B. Tang, and A.L. Zhang, *J. Alloys Compd.* 583, 162 (2014).
17. B. Gorr, M. Azim, H.-J. Christ, T. Mueller, D. Schliephake, and M. Heilmaier, *J. Alloys Compd.* 624, 270 (2015).
18. B. Gorr, F. Mueller, H.-J. Christ, T. Mueller, H. Chen, A. Kauffmann, and M. Heilmaier, *J. Alloys Compd.* 688, 468 (2016).
19. T.M. Butler, K.J. Chaput, J.R. Dietrich, and O.N. Senkov, *J. Alloys Compd.* 729, 1004 (2017).
20. C.-H. Chang, M.S. Titus, and J.W. Yeh, *Adv. Eng. Mater.* 20, 1700948 (2018).
21. H.J. Park, Y.S. Na, S.H. Hong, J.T. Kim, Y.S. Kim, K.R. Lim, J.M. Park, and K.B. Kim, *Met. Mater. Int.* 22, 551 (2016).
22. E. Jumaev, S.H. Hong, J.T. Kim, H.J. Park, Y.S. Kim, S.C. Mun, J.-Y. Park, G. Song, J.K. Lee, B.H. Min, T. Lee, and K.B. Kim, *J. Alloys Compd.* 777, 828 (2019).
23. M.J. Kim, G.C. Kang, S.H. Hong, H.J. Park, S.C. Mun, G. Song, and K.B. Kim, *J. Mater. Sci. Technol.* 57, 131 (2020).
24. J.W. Yeh, *JOM* 65, 1759 (2013).
25. M.C. Gao, J.W. Yeh, P.K. Liaw, and Y. Zhang, *High-Entropy Alloys: Fundamentals and Applications* (New York: Springer, 2016), pp. 8–12.
26. L. Qi and D.C. Chrzan, *Phys. Rev. Lett.* 112, 115503 (2014).
27. N.N. Guo, L. Wang, L.S. Luo, X.Z. Li, Y.Q. Su, J.J. Guo, and H.Z. Fu, *Mater. Des.* 81, 87 (2015).
28. S. Sheikh, S. Shafeie, Q. Hu, J. Ahlström, C. Persson, J. Veselý, J. Zýka, and U. Klement, *J. Appl. Phys.* 120, 164902 (2016).
29. H. Huang, Y. Wu, J. He, H. Wang, X. Liu, K. An, W. Wu, and Z. Lu, *Adv. Mater.* 29, 1701678 (2017).
30. V. Soni, O.N. Senkov, B. Gwalani, D.B. Miracle, and R. Banerjee, *Sci. Rep.* 8, 8816 (2018).
31. W. Guo, B. Liu, Y. Liu, T. Li, A. Ju, Q. Fang, and Y. Nie, *J. Alloys Compd.* 776, 428 (2019).
32. O.N. Senkov and S.L. Semiatin, *J. Alloys Compd.* 649, 1110 (2019).
33. G.W. Goward and L.W. Cannon, *J. Eng. Gas Turbines Power* 110, 150 (1988).
34. A.U. Seybolt, *Trans. AIME* 200, 770 (1954).
35. R.P. Elliot, *Trans. Am. Soc. Met.* 52, 900 (1960).
36. R. Bryant, *J. Less Common Met.* 4, 62 (1962).
37. W.D. Klopp, *JOM* 21, 23 (1969).
38. H. Jehn and E. Olzi, *J. Less Common Met.* 27, 297 (1972).